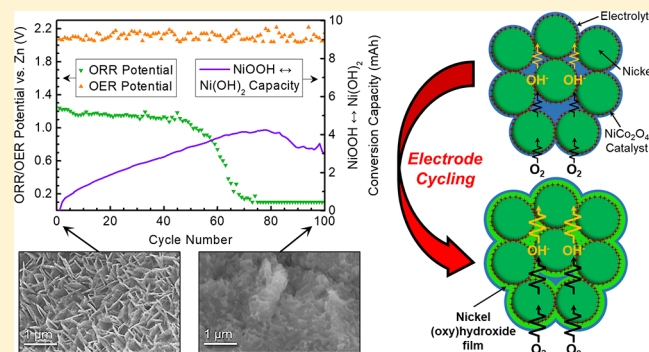


New Interpretation of the Performance of Nickel-Based Air Electrodes for Rechargeable Zinc–Air Batteries

Zachary P. Cano,¹ Moon Gyu Park, Dong Un Lee,[†] Jing Fu, Hao Liu, Michael Fowler,¹ and Zhongwei Chen^{*1}

Department of Chemical Engineering, University of Waterloo, 200 University Avenue West, Waterloo, Ontario N2L 3G1, Canada

ABSTRACT: Rechargeable zinc–air batteries with high energy density, cycle life, and calendar life require corrosion-resistant support materials in the air electrode. Nickel-based air electrodes have shown promise in this regard as a substitute for conventional carbon-based air electrodes, but their performance in zinc–air batteries has not been studied in-depth. Specifically, the effect of the nickel (oxy)hydroxide passivating film on the electrode's catalytic performance and durability requires investigation. To fill this research gap, a method involving electrochemical estimation of the nickel (oxy)hydroxide film capacity was used to link the growth of the film to performance losses experienced on the air electrode after battery cycling. The main cause of voltage loss was the nickel (oxy)hydroxide film growing otop of and inside the catalyst-coated nickel aggregates. This resulted in significant activation and mass transfer losses, where the latter losses were caused by the film growing otop of the catalyst and accounted for at least 65% of the total voltage degradation at 10 mA cm⁻². Potential modifications to the electrode structure which could mitigate these voltage losses are discussed, including reducing the nickel particle aggregate size, using high-aspect ratio catalysts, and physically separating the catalyst and nickel particles with nonfilm-forming conductive additives.



INTRODUCTION

Batteries are an important component of future energy networks due to their ability to store energy in mobile or stationary systems and balance the supply and demand of power with fast response times.^{1,2} Rechargeable lithium-ion batteries are currently the most popular technology for these applications due to their high energy density, power density, cycle life and efficiency. However, to support a wider range of applications, batteries with lower-cost materials, higher volumetric energy density and higher safety are desired. Zinc–air batteries are very promising in this regard,³ with a projected system-level cost less than \$100 USD kWh⁻¹,⁴ a cell-level volumetric energy density as high as 1400 Wh L⁻¹,⁵ and inherently safe operation.^{6,7} In recent years, several companies have developed rechargeable zinc–air batteries for grid-level energy storage. However, these battery systems require a circulating electrolyte and/or electrolyte filtering to maintain long-term performance, which increases complexity, decreases efficiency, and limits the system-level energy density.⁸ Zinc–air batteries with a compact cell design and static electrolyte, on the other hand, could meet energy storage needs where space is a constraint such as electric vehicles⁹ or urban energy grids.¹⁰ Therefore, electrode materials that offer high durability for rechargeable zinc–air batteries with static electrolytes should be explored.

Because of the kinetically slow oxygen reduction reaction (ORR) and oxygen evolution reaction (OER), the power and

energy efficiency of a rechargeable zinc–air battery is highly dependent on the catalytic performance of the air electrode.¹¹ The development of bifunctional catalysts that can efficiently facilitate the ORR and OER with low overpotentials, while also remaining stable over hundreds of charge–discharge cycles in alkaline electrolytes, is currently the most intense area of research.^{12–16} This research includes surface and structure engineering of bifunctional catalysts to optimize their oxygen binding energies and cohesive strength for efficient and stable ORR and OER.^{17–20} However, relatively little attention has been paid to the support and/or current-collector materials of the air electrode. In fact, a large amount of research on catalysts for rechargeable zinc–air batteries has been conducted using commercial gas diffusion layers made of carbon and designed for polymer electrolyte membrane fuel cells.^{21–26} Carbon and graphite powders are also traditionally used as the conductive catalyst support for fuel cells and primary zinc–air batteries due to their low cost, relatively good activity for the ORR and their widely tunable surface area and porosity.^{27–31}

Unfortunately, carbon-based air electrodes are susceptible to rapid corrosion at the high oxidizing potentials experienced at the air electrode during charging (OER) of a zinc–air

Received: June 29, 2018

Revised: August 8, 2018

Published: August 14, 2018

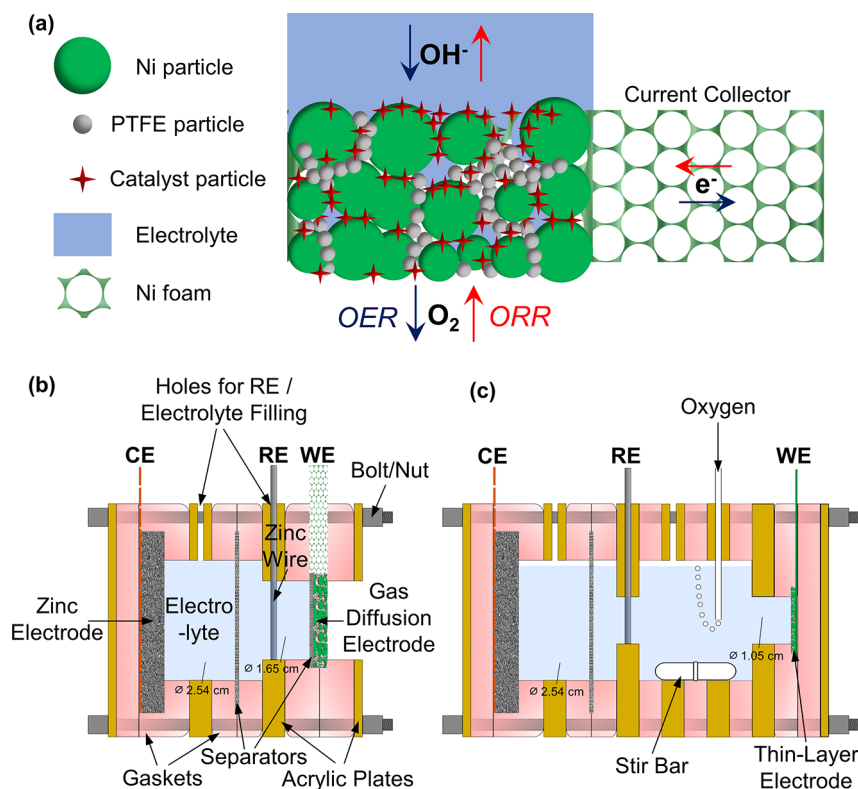


Figure 1. (a) Schematic depiction of single-layer nickel-based gas diffusion electrode (particles enlarged relative to the nickel foam pores for clarity), and schematic representations (side-view) of three-electrode cells for performance evaluation of (b) nickel-based gas diffusion electrode and (c) nickel-based thin-layer electrode as the working electrode (WE). A porous zinc electrode and zinc wire were employed as the counter electrode (CE) and reference electrode (RE), respectively.

battery.^{32–37} The standard potential of carbon oxidation in alkaline electrolyte (pH of 14) is -0.78 V vs SHE (0.48 V vs Zn/ZnO), which is much lower than the ORR/OER equilibrium potential (0.40 V vs SHE, 1.66 V vs Zn/ZnO).^{38,39} Therefore, although graphitization of carbon improves its corrosion resistance,^{34,37,40–43} corrosion is thermodynamically favored even at the open circuit voltage of zinc–air batteries. Also, the formation of carbonate (CO_3^{2-}) ions from carbon corrosion can combine with CO_2 poisoning from the outside atmosphere to hasten the precipitation of K_2CO_3 in the air electrode pores, which can block catalyst sites and limit oxygen diffusion.³⁷ This is an increasingly challenging problem in zinc–air cell designs which maximize energy density by lowering the volume of electrolyte, since CO_3^{2-} saturation and precipitation would occur more quickly. Therefore, rechargeable zinc–air batteries with high energy density, long cycle life, and long calendar life require more corrosion-resistant materials in the air electrode.

Metal-based air electrodes can offer much higher corrosion resistance due to their ability to form a passivating film on their surface, which greatly reduces the metal oxidation rate.⁸ However, relatively few investigations have focused on metal-based air electrodes for rechargeable metal-air batteries. Silver-based air electrodes with increased stability relative to carbon-based air electrodes have been demonstrated for alkaline fuel cells and lithium–air batteries,^{44–46} although their high cost likely makes them impractical for low-cost zinc–air batteries. A promising air electrode based on less expensive nickel metal was demonstrated by Price and co-workers^{47,48} for flow-based rechargeable zinc–air batteries. Their fabrication technique involved the pressing of a slurry composed of nickel powder

and polytetrafluoroethylene (PTFE) onto a Ni foam support, followed by dip-coating in a catalyst precursor solution. The resulting bifunctional air electrode demonstrated stable potentials after 50 charge–discharge cycles at a relatively high current density (50 mA cm^{-2}). The oxidized nickel in the (oxy)hydroxide passivating layer alternated between the 2+ and 3+ states ($\text{Ni}(\text{OH})_2$ and NiOOH) during the start of discharging and charging, respectively, which was reported as beneficial to its efficiency due to the lower overpotential of these reactions relative to the ORR and OER.⁴⁷ Because of their relatively high stability, nickel-based air electrodes have been adopted by some research groups for demonstration of novel bifunctional catalysts.^{49–52}

Despite their promising performance, the degradation mechanism of nickel-based air electrodes after extended cycling has not been discussed in the literature. This is an important consideration, since voltage losses after battery cycling might be mistakenly attributed to degradation of the catalyst particles instead of possible material changes on the supporting nickel electrode. The electrode structure is presumed to resemble the “flooded agglomerate” model of typical carbon-based air electrodes,^{53–56} with electrolyte-flooded agglomerates of catalyst-coated nickel particles bound by a network of hydrophobic channels established by the PTFE binder. For the ORR, oxygen gas diffuses through the hydrophobic channels, dissolves in an electrolyte film surrounding the hydrophilic agglomerates, and diffuses further within the agglomerate until it is reduced at various catalyst sites. However, a key dynamic which does not apply to carbon-based air electrodes is the influence of the (oxy)hydroxide passivating layer on this mechanism. Whether this dynamic

contributes to voltage losses of zinc–air batteries with nickel-based air electrodes, and if so, to what extent, needs to be understood for extending battery durability.

To address this question in this work, nickel-based air electrodes were fabricated and investigated with a series of cyclic galvanostatic and potentiodynamic polarization experiments. The structure of the electrode before and after cycling was characterized to confirm the presence of a passivating nickel (oxy)hydroxide film. A multistep discharge method was used to estimate the growth of the nickel (oxy)hydroxide passivating film, which was linked to dynamic potential losses at the air electrode. Relative contributions of ohmic, activation and mass transfer potential losses were evaluated at a current density of 10 mA cm^{-2} , which is commonly used for evaluation of static-electrolyte rechargeable zinc–air batteries. The results provide strong evidence of a degradation mechanism for nickel-based air electrodes which is distinct from degradation of the catalyst itself. This insight will aid in the design of more robust bifunctional metal-based air electrodes for long-lasting rechargeable zinc–air batteries.

■ EXPERIMENTAL SECTION

Electrode Preparation and Characterization. The preparation procedure for the nickel-based gas diffusion electrode was adapted from Price et al.⁴⁸ Nickel foam (110 pores per inch, 42 mg cm^{-2} , 1.7 mm thick) was used as the electrode support and current collector. Prior to electrode rolling, the nickel foam was ultrasonically treated in acetone for 20 min, etched in 1 mol L^{-1} HCl at $80 \text{ }^\circ\text{C}$ for 1 h, rinsed and ultrasonically treated in deionized water for 15 min, rinsed with isopropyl alcohol (IPA) and finally dried in air. To prepare the electrode slurry, nickel powder (Sigma-Aldrich, Product #266981) with an average particle size of approximately $3 \text{ }\mu\text{m}$ was added to a vial together with a 50/50 mixture of IPA and deionized water. 60 wt % PTFE emulsion (Sigma-Aldrich, Product #665800) was then added dropwise to the vial while stirring and the slurry was ultrasonically mixed for 30 min. The slurry was blended in a planetary mixer for 5 min to bind the nickel powder with the PTFE. After pouring out excess liquid, the blended mass was placed onto aluminum foil and rolled into a flat sheet with the same area as the nickel foam. The nickel/PTFE sheet was then pressed into the nickel foam and rolled to a combined thickness of $1000 \text{ }\mu\text{m}$ using fixed-width rollers. The dried nickel/PTFE slurry had a PTFE content of 30%, and the slurry mass loading in the nickel foam was approximately 180 mg cm^{-2} . After allowing the rolled electrode to dry overnight, the electrode was heated at $350 \text{ }^\circ\text{C}$ in air for 30 min and then immersed in a cobalt/nickel nitrate precursor solution for 5 min. The precursor solution consisted of 2 mol L^{-1} cobalt(II) nitrate (Sigma-Aldrich, Product #239267) and 1 mol L^{-1} nickel(II) nitrate (Sigma-Aldrich, Product #72253) dissolved in a 60/40 mixture of H_2O /IPA. The electrode was dried in air at room temperature for approximately 3 h and finally was heated at $350 \text{ }^\circ\text{C}$ in air for 3 h to convert the nitrates into the nickel cobalt oxide (NiCo_2O_4) spinel phase.

The final gas diffusion electrode (depicted in Figure 1a) had a diameter of 1.9 cm and included an approximately 2 cm long extended piece of the nickel foam current collector which acted as the working electrode connection. A thin-layer electrode was also fabricated by rolling an identical nickel/PTFE mixture down to $150 \text{ }\mu\text{m}$ (dry slurry mass of approximately 75 mg cm^{-2}), pressing it onto a nickel foil current collector and

carrying out the same heating and dip-coat treatment as described above. Morphological characterization of the gas diffusion electrode was conducted with a Zeiss LEO 1530 field emission scanning electron microscope (SEM). X-ray diffraction (XRD) was conducted on a MiniFlex 600 Rigaku instrument, and X-ray photoelectron spectroscopy (XPS) was conducted on a Thermal Scientific K-Alpha XPS spectrometer.

Cell Design. Two cell designs (Figure 1b,c) containing a combination of acrylic plates and silicone gaskets fastened together with bolts and nuts were employed for electrochemical testing. Each design utilized a three-electrode configuration including a porous zinc counter electrode and zinc wire reference electrode. Unlike a two-electrode configuration, the cells employed here ensured that any possible degradation of the porous zinc electrode during cycling would not affect the potential measurement at the air electrode.⁸ The electrolyte in each experiment was an aqueous solution of 6 mol L^{-1} KOH prepared from distilled and deionized water. The electrolyte was also presaturated with zinc oxide (ZnO) to improve cyclability of the zinc electrode and to ensure that the potential of the zinc wire reference electrode maintained a stable equilibrium potential. Porous zinc electrodes were prepared via cathodic electrodeposition from a fresh electrolyte with the same composition as above onto a Cu mesh current collector at a potential of $-300 \text{ mV vs Zn/ZnO}$.⁵⁷ The capacities of these zinc electrodes were at least 10 times the capacity required for discharge (i.e., ORR) steps in the cycling procedures described below.

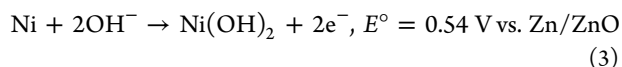
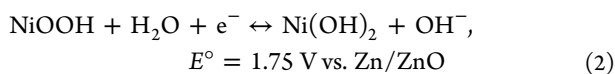
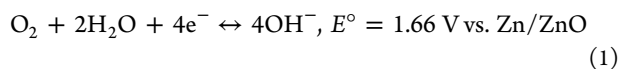
The cell depicted in Figure 1b was employed for electrochemical testing of the gas diffusion electrode. The electrode was exposed to the electrolyte on the inner side and ambient air on the outer side through 1.65 cm diameter circular holes in the adjacent gaskets and plates. The Ni/PTFE slurry-deposited side of the electrode faced the air and the nonslurry-deposited side faced the electrolyte. A microporous polypropylene separator (Celgard 5550) separated the zinc counter electrode from the gas diffusion electrode. An additional microporous separator was also placed directly adjacent to the gas diffusion electrode on the electrolyte side; this ensured that oxygen gas evolved during OER exited through the air-side of the cell rather than bubbling into the electrolyte. However, it should be noted that this separator placement caused slightly higher OER potentials (approximately 0.1 V higher) to be observed, possibly due to some oxygen bubbles becoming stuck between the electrode surface and separator and reducing electrolyte coverage of the electrode. The distance between the zinc wire reference electrode and gas diffusion electrode was approximately 2 mm.

The cell depicted in Figure 1c was used for electrochemical testing of the thin-layer electrode. The electrode in this cell was not exposed to the air; oxygen exposure was instead provided via dissolved oxygen in an oxygen-saturated electrolyte. A magnetic stir bar in the cell was rotated at 500 rpm to facilitate electrolyte wetting and oxygen transport to the electrode, which was exposed to the electrolyte through a 1.05 cm diameter opening. As will be discussed in more detail, this design was mainly employed to avoid time-sensitive potential losses caused by electrolyte flooding into the gas pores of the thicker gas diffusion electrode. A distance over 1 cm separated the zinc wire reference electrode and thin-layer electrode in this cell; however, IR-compensation was employed for polarization experiments using both designs to negate any associated potential drops in the electrolyte.

Table 1. Galvanostatic Cycling Procedure for Nickel-Based Gas Diffusion Electrode

step	operation	duration/end condition	dominant reaction
1	rest	5 min	
2	reduction @ 10 mA cm ⁻²	cut-off @ 1.3 V	eq 2 (forward)
3	reduction @ 10 mA cm ⁻²	15 min or cutoff @ 0.1 V	eq 1 (forward)
4	rest	5 min	
5	oxidation @ 10 mA cm ⁻²	cut-off @ 1.95 V	eq 2 (reverse), eq 3
6	oxidation @ 10 mA cm ⁻²	17 min	eq 1 (reverse)
7	loop to step 1		

Electrochemical Testing. Galvanostatic charge/discharge cycling of the gas diffusion electrode was conducted on a Neware BTS3000 battery tester, while galvanostatic electrochemical impedance spectroscopy (EIS) and potentiodynamic polarization experiments were conducted on a Bio-Logic VSP potentiostat. All potentials herein are reported relative to the zinc wire reference electrode (Zn/ZnO). Several reactions occurred on the air electrodes in each experiment, including ORR and OER (eq 1), NiOOH reduction and Ni(OH)₂ oxidation (eq 2) and nickel metal oxidation (eq 3). Each reaction and its standard equilibrium potential³⁹ relative to Zn/ZnO in alkaline electrolyte is provided below.



Galvanostatic cycling was used to evaluate the rechargeability of the nickel-based gas diffusion electrode at 10 mA cm⁻². The exact test sequence is shown in Table 1 and is also demonstrated graphically in Figure 2. Unlike a typical cycling experiment, two-step reduction (corresponding to battery discharge) and two-step oxidation (battery charge) cycles were employed to separately evaluate the oxygen reactions (eq 1)

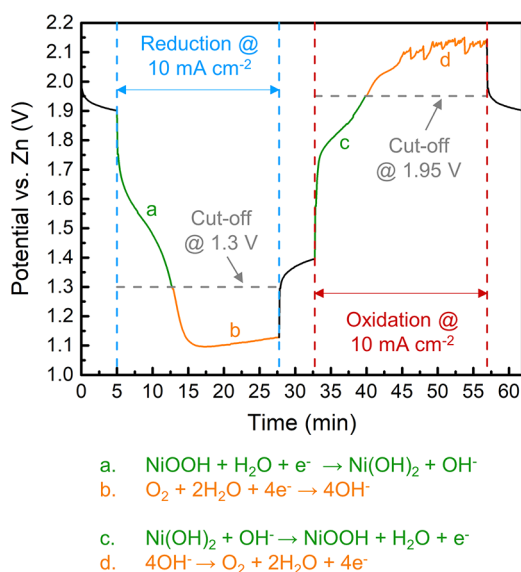


Figure 2. Graphical demonstration of two-step reduction and two-step oxidation cycles and the dominant reactions occurring at each step.

and the NiOOH/Ni(OH)₂ reactions (eq 2). This was possible due to the relatively smaller overpotentials of the NiOOH/Ni(OH)₂ reactions, which enabled cutoff potentials used in the first step of the reduction or oxidation cycle to indicate when these reactions were approximately completed. Since the ORR potential was never higher than 1.3 V vs Zn and the OER potential was never lower than 1.95 V vs Zn at 10 mA cm⁻², cutoff potentials of 1.3 and 1.95 V vs Zn were used respectively during reduction and oxidation to determine the approximate capacity of eq 2. This capacity is assumed to be proportional to the volume or thickness of the nickel (oxy)hydroxide film in each cycle. Therefore, changes of the NiOOH/Ni(OH)₂ capacity could be compared with changes of the ORR or OER overpotentials to determine if there is a correlation between the film growth and the electrode's catalytic performance. After the electrode potential passed these cutoff voltages, reduction continued for 15 min to evaluate the ORR potential or 17 min to evaluate the OER potential. Extra time was allocated to the oxidation step to ensure the Zn counter electrode's capacity did not rapidly drop during cycling, since some of the deposition current at the Zn electrode is lost to hydrogen evolution. While the hydrogen quantity evolved from the Zn electrode during this step was not quantified, 2 min extra was determined to be suitable based on visual observation that the Zn electrode's size did substantially change after the cycling procedure. During the rest steps in this procedure, the gradual recovery of the open circuit potential as shown in Figure 2 can be attributed to the slow rebalancing of the oxygen and/or hydroxide concentration gradients established during oxidation or reduction steps.^{58,59}

In the next electrochemical experiment, galvanostatic cycling was employed together with galvanostatic EIS on the gas diffusion electrode (Table 2). This was used to measure changes of the ohmic resistance of the cell and impedance characteristics of the ORR as cycling progressed. For each cycle, a 60 min reduction step at 10 mA cm⁻² was used prior to each EIS measurement to ensure the NiOOH film was fully reduced to Ni(OH)₂ and that the air electrode had reached a stable potential. The galvanostatic EIS measurement was conducted at 10 mA cm⁻² with a frequency range from 100 kHz to 10 mHz and an amplitude of 2 mA cm⁻².

Cyclic potentiodynamic polarization experiments were then conducted on the gas diffusion and thin-layer electrodes according to the protocol outlined in Table 3. To evaluate the effect of (oxy)hydroxide film growth on the ORR kinetics, the polarization curves were recorded after various cumulative times of oxidation at 2.2 V vs Zn. Like the previous experiments, multistep oxidation and reduction reactions were applied to distinguish the oxygen reactions from the NiOOH/Ni(OH)₂ reactions. An additional galvanostatic reduction step at 1 mA cm⁻² with an appropriate cutoff voltage and a following potentiostatic reduction step at the

Table 2. Galvanostatic Cycling and EIS Procedure for Nickel-Based Gas Diffusion Electrode

step	operation	duration	dominant reactions
1	rest	5 min	
2	reduction @ 10 mA cm^{-2}	60 min	eq 1 (forward), eq 2 (forward)
3	reduction @ 10 mA cm^{-2} with EIS	~30 min	eq 1 (forward)
4	rest	5 min	
5	oxidation @ 10 mA cm^{-2}	90 min	eq 1 (reverse), eq 2 (reverse), eq 3
6	loop to step 1		

Table 3. Cyclic Potentiodynamic Polarization Procedure for the Nickel-Based Gas Diffusion Electrode (GDE) and Thin-Layer Electrode (TLE)

step	operation	duration/end condition	dominant reaction
1	rest	5 min	
2	reduction @ 10 mA cm^{-2}	cut-off @ 1.3 V (GDE), @ 1.2 V (TLE)	eq 2 (forward)
3	reduction @ 1 mA cm^{-2}	cut-off @ 1.35 V (GDE), @ 1.325 V (TLE)	eq 2 (forward)
4	reduction @ 1.35 V vs Zn (GDE), @ 1.325 V vs Zn (TLE)	60 min	eq 1 (forward), eq 2 (forward)
5	IR-corrected potentiodynamic polarization	1.35 to 0.875 V @ 0.25 mV s^{-1} (GDE), 1.325 to 0.8 V @ 0.1 mV s^{-1} (TLE)	eq 1 (forward)
6	rest	5 min	
7	oxidation @ 10 mA cm^{-2}	cut-off @ 1.95 V vs Zn	eq 2 (reverse)
8	oxidation @ 2.2 V vs Zn	variable duration	eq 1 (reverse), eq 2 (reverse), eq 3
9	loop to step 1		

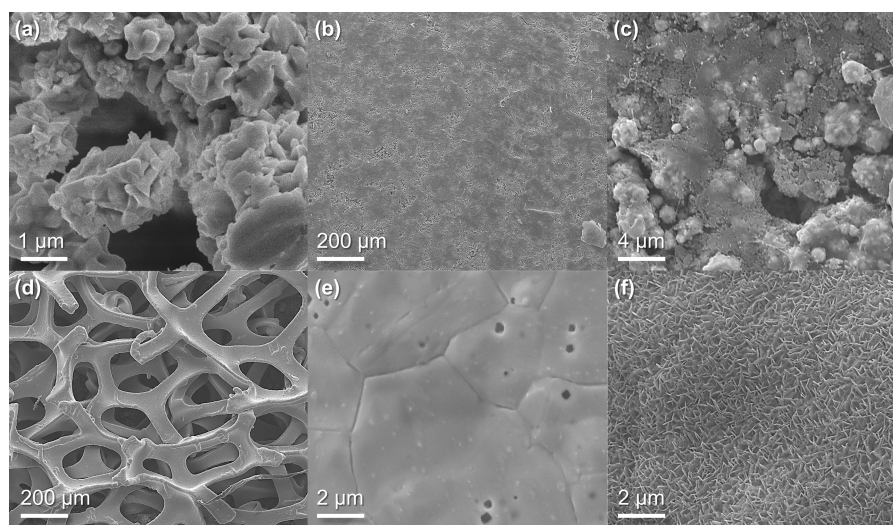


Figure 3. SEM images of (a) the nickel particle morphology; the Ni/PTFE slurry-deposited side of the electrode at (b) low magnification, and (c) high magnification; the non-slurry side of the electrode at (d) low magnification, (e) high magnification, and (f) high magnification after deposition of the NiCo_2O_4 catalyst.

cutoff voltage were applied to ensure that NiOOH reduction and any associated capacitive currents⁶⁰ were fully completed prior to recording the ORR polarization curves. IR-correction to the polarization curves was applied using ohmic resistance measurements at the starting potential and 85% correction to the applied potentials. The remaining 15% correction was applied to the polarization data afterward.

RESULTS AND DISCUSSION

The morphology of the nickel particles used to fabricate the nickel-based air electrodes are shown in Figure 3a. Carbonyl nickel particles were selected due to their rough texture which provided a high surface area for catalyst deposition. The Ni/

PTFE slurry-deposited side of the electrode is shown at low magnification in Figure 3b, revealing a smooth surface with several micropores allowing for gas diffusion. The higher magnification SEM image in Figure 3c shows the PTFE-bonded nickel particles more clearly. Figure 3d,e show the nickel foam morphology at low and high magnification on the non-slurry side of the electrode. After the Co/Ni nitrate dip-coating procedure, the NiCo_2O_4 catalyst particles displayed a nanoflake structure (Figure 3f).

Galvanostatic cycling test results for the gas diffusion electrode are provided in Figure 4. The electrode was subjected to 100 cycles of the test protocol outlined in Table 1, with the potential variations for cycles 1–10, 51–60

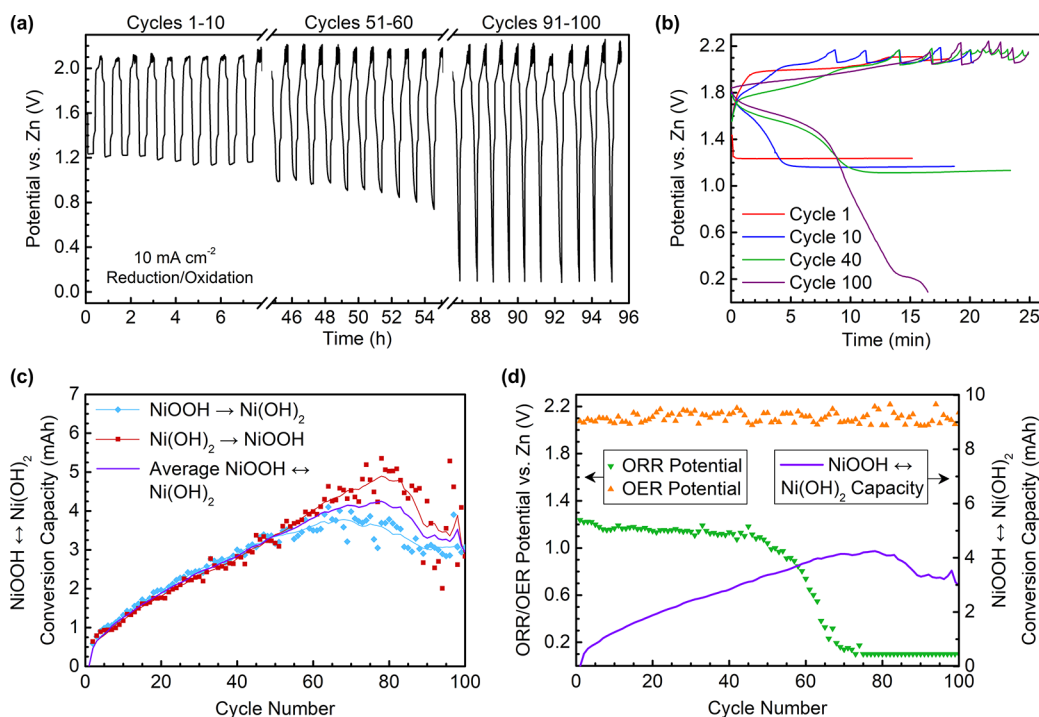


Figure 4. Galvanostatic cycling (procedure per Table 1) for nickel-based gas diffusion electrode: (a) galvanostatic cycling potentials, (b) oxidation and reduction transients at different cycle numbers, (c) NiOOH \rightarrow Ni(OH)₂ and Ni(OH)₂ \rightarrow NiOOH conversion capacities with 10-point adjacent-average smoothed lines, and (d) ORR/OER potentials and average NiOOH/Ni(OH)₂ capacity as a function of cycle number.

and 91–100 shown in Figure 4a. The ORR potential at the end of each cycle decreased from 1.24 to 1.17 V vs Zn within the first 10 cycles, and fell further to 1.04 V by the end of the 50th cycle. After the 50th cycle, the ORR potential started to decline more rapidly, and after approximately 75 cycles it consistently fell below the lower cutoff voltage of 0.1 V vs Zn. The OER potential displayed fluctuating potentials within each cycle, which has been previously observed^{48,61} and could be explained by the growth and detachment of oxygen bubbles disrupting the solid/electrolyte interface. However, the OER potentials remained relatively consistent throughout the 100 cycles. Therefore, the remainder of the investigation was focused on uncovering the origin(s) of ORR kinetic losses.

Figure 4b displays oxidation and reduction transients at various cycle numbers. For the first reduction and oxidation cycles, the electrode potential quickly attained stable values in the expected potential ranges for ORR and OER, indicating that very little nickel oxidation had yet occurred. However, subsequent cycles displayed an initial period of lower overpotentials before a stabilized ORR or OER potential was established. The profiles for the 10th, 40th, and 100th cycles show that this low-overpotential period became increasingly longer as cycling progressed, indicating a continual increase of the conversion capacity between Ni(OH)₂ and NiOOH. This demonstrates the importance of using sufficiently long cycles for ORR/OER evaluation of nickel-based air electrodes, since the NiOOH/Ni(OH)₂ conversion reactions must be completed before measuring the oxygen reaction potentials.

The capacities of the NiOOH \rightarrow Ni(OH)₂ conversion reaction (measured by the capacity of the reduction step before the potential fell below 1.3 V vs Zn) and the Ni(OH)₂ \rightarrow NiOOH conversion reaction (measured by the capacity of the oxidation step before the potential rose above 1.95 V vs Zn) are shown as a function of cycle number in Figure 4c. Both

capacity measurements rose quickly above an assumed initial value of zero during the first five cycles, and then continued to rise almost linearly at a more gradual rate. After the 50th cycle, the measured capacities started to diverge, with the NiOOH \rightarrow Ni(OH)₂ conversion reaction displaying apparently lower values. This was likely caused by the rapidly decreasing ORR activity, since the potential above 1.3 V (although mainly attributable to the NiOOH \rightarrow Ni(OH)₂ conversion reaction) may be partially dictated by the ORR activity. After the 80th cycle, both measured capacities appeared to reach a maximum, suggesting that Ni (oxy)hydroxide growth stopped at this point. The ORR and OER potentials observed at the end of each cycle, along with the average measured NiOOH/Ni(OH)₂ capacity during each cycle, are plotted together in Figure 4d. Although the ORR potential decreased and the NiOOH/Ni(OH)₂ capacity increased during the 100 cycles, no direct correlation between the two measurements as a function of cycle number was evident here.

To view morphological changes which may have contributed to the steep drop in ORR activity, SEM images of the gas diffusion electrode were taken before and after 100 cycles of the protocol outlined in Table 1. Parts a and b of Figure 5 respectively show the non-slurry and slurry-deposited side of the electrode before cycling, and parts c and d of Figure 5 respectively show the non-slurry and slurry-deposited side of the electrode after 100 cycles. Before cycling, the NiCo₂O₄ catalyst flakes are clearly visible on both sides of the electrode. However, after 100 cycles, both sides of the electrode appeared to be covered by a spongy film and the NiCo₂O₄ flakes were no longer visible, suggesting the film grew overtop of the catalyst.

XRD spectra of the electrode surface before cycling and after 10 and 100 cycles were recorded to try to identify the material phases observed visually in SEM. The largest peaks observed

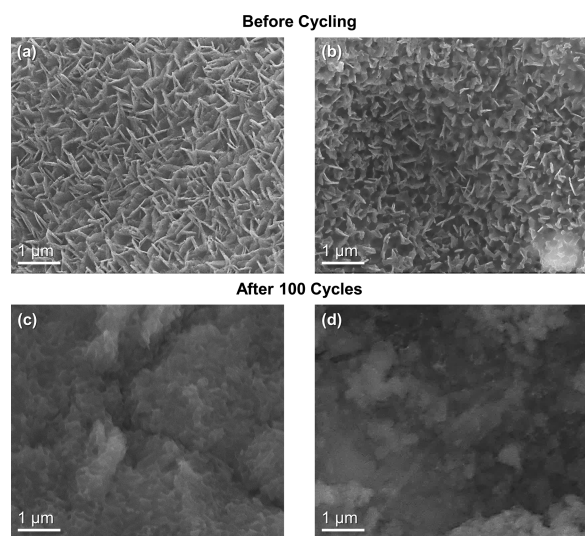


Figure 5. SEM images of the nickel-based gas diffusion electrode: (a) non-slurry side and (b) slurry-deposited side before cycling; (c) non-slurry side and (d) slurry-deposited side after 100 galvanostatic oxidation/reduction cycles (Table 1).

on all samples were those of metallic nickel (JCPDS #04-0850), as shown in Figure 6. Smaller peaks corresponding to

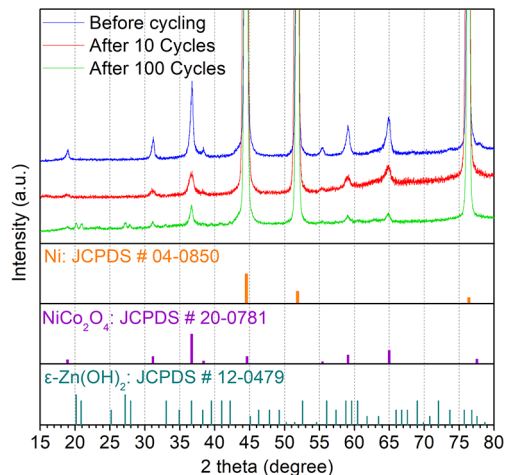


Figure 6. XRD spectra of the nickel-based gas diffusion electrode surface before cycling and after 10 and 100 galvanostatic oxidation/reduction cycles (Table 1).

NiCo_2O_4 (JCPDS #20-0781) were also observed on each sample, and their intensities became progressively smaller after cycling, which is consistent with observation in Figure 5 of the NiCo_2O_4 catalyst becoming covered by the overlying film. However, diffraction peaks corresponding to the $\text{Ni}(\text{OH})_2$ or NiOOH phases which were expected to constitute the film observed in SEM were not detected. This could be explained by previous observations that nickel (oxy)hydroxides grown electrochemically have poor crystalline ordering.⁶² After 100 cycles, new peaks corresponding to the metastable $\epsilon\text{-Zn}(\text{OH})_2$ phase were observed. This phase likely resulted from precipitation of the $\text{Zn}(\text{OH})_4^{2-}$ ion from the electrolyte.^{63,64}

To further study the chemical changes of the nickel-based air electrode surface, XPS was performed before and after 10 and 100 cycles of the protocol outlined in Table 1. As shown in the survey spectra (Figure 7a), peaks corresponding to Co, Ni, and

O (from the NiCo_2O_4 catalyst) and to C and F (from the PTFE binder) were observed before cycling. After cycling, the Co peaks became progressively weaker while the Ni peaks became stronger especially after 100 cycles. Peaks corresponding to residual Zn from the ZnO-saturated electrolyte were also present after cycling. Figure 7b shows the evolution of the electrode surface's elemental composition before and after cycling. The most important observation was a dramatic reduction of the Co content after cycling, indicating a reduced presence of the NiCo_2O_4 catalyst flakes on the surface which is consistent with the SEM and XRD results. Concurrently, the Ni content increased after 100 cycles, and would have also increased after 10 cycles if the quantification of residual Zn from the electrolyte was ignored. This, together, with the progressively increased O content after cycling, indicates the growth of an oxidized and/or hydrated Ni film overtop of the NiCo_2O_4 catalyst. The reduction of C and F were likely caused by the growing Ni-rich film overtop of the PTFE binder. Also, the fact that the Zn content only slightly increased between 10 and 100 cycles means that it was unlikely to have played a major role in the severe ORR potential losses observed between cycles 50 and 70 in Figure 4, even if it had precipitated on the electrode surface during cycling and not after removal of the electrode from the cell.

The high-resolution XPS spectra of the Ni 2p and O 1s peaks were investigated and deconvoluted to gain better insight into the chemical state of the Ni-rich film which grew on the electrode surface after cycling. The Ni 2p spectra, for which only the $2p_{3/2}$ spectra were deconvoluted, are presented in Figure 7c. The spectrum recorded before cycling was fitted with a multiplet envelope of three main peaks and two satellite peaks assigned to NiCo_2O_4 .⁶⁷ After 10 cycles, the main peak in the $2p_{3/2}$ spectral pattern was noticeably broadened, which was well-fitted by adding the two major peaks of the multiplet envelope for $\text{Ni}(\text{OH})_2$ ⁶⁷ and reducing the main NiCo_2O_4 peak intensities. This confirms the growth of a Ni (oxy)hydroxide film (observed as $\text{Ni}(\text{OH})_2$ here, since the electrode was analyzed after the electrochemical reduction steps in Table 1) overtop of the NiCo_2O_4 catalyst in the early cycling stages. The spacing and relative sizes and shapes of the deconvoluted NiCo_2O_4 peaks remained largely unchanged in the optimized fitting, meaning that their chemical states did not appear to be altered after growth of the $\text{Ni}(\text{OH})_2$ film. After 100 cycles, the main peak and satellite peak structures became larger and significantly shifted to higher binding energies. This spectrum was fitted by adding a main peak around 857 eV corresponding to NiOOH ^{68–70} and a new satellite peak around 863 eV, using fixed full width at half-maximum values previously reported for electrochemically prepared $\gamma\text{-NiOOH}$.⁷¹ The presence of NiOOH together with $\text{Ni}(\text{OH})_2$ after 100 cycles means that the Ni (oxy)hydroxide film was not fully reduced to $\text{Ni}(\text{OH})_2$ after it grew significantly thick, which could mean the film continued to grow even after its capacity appeared to plateau in Figure 4c.

The high-resolution O 1s spectra are shown in Figure 7d. The first spectrum before cycling was deconvoluted into two peaks corresponding to lattice oxides (529.7 eV) and defective oxides (531.3 eV) in the NiCo_2O_4 catalyst.^{67,72,73} After 10 cycles, the low-binding energy peak of the spectrum decreased while the high-binding energy peak increased, which was fitted by adding a sharper hydroxide peak at 531.3 eV.^{73,74} An additional peak at 532.4 eV corresponding to physisorbed or intercalated water^{75,76} was also necessary to produce an

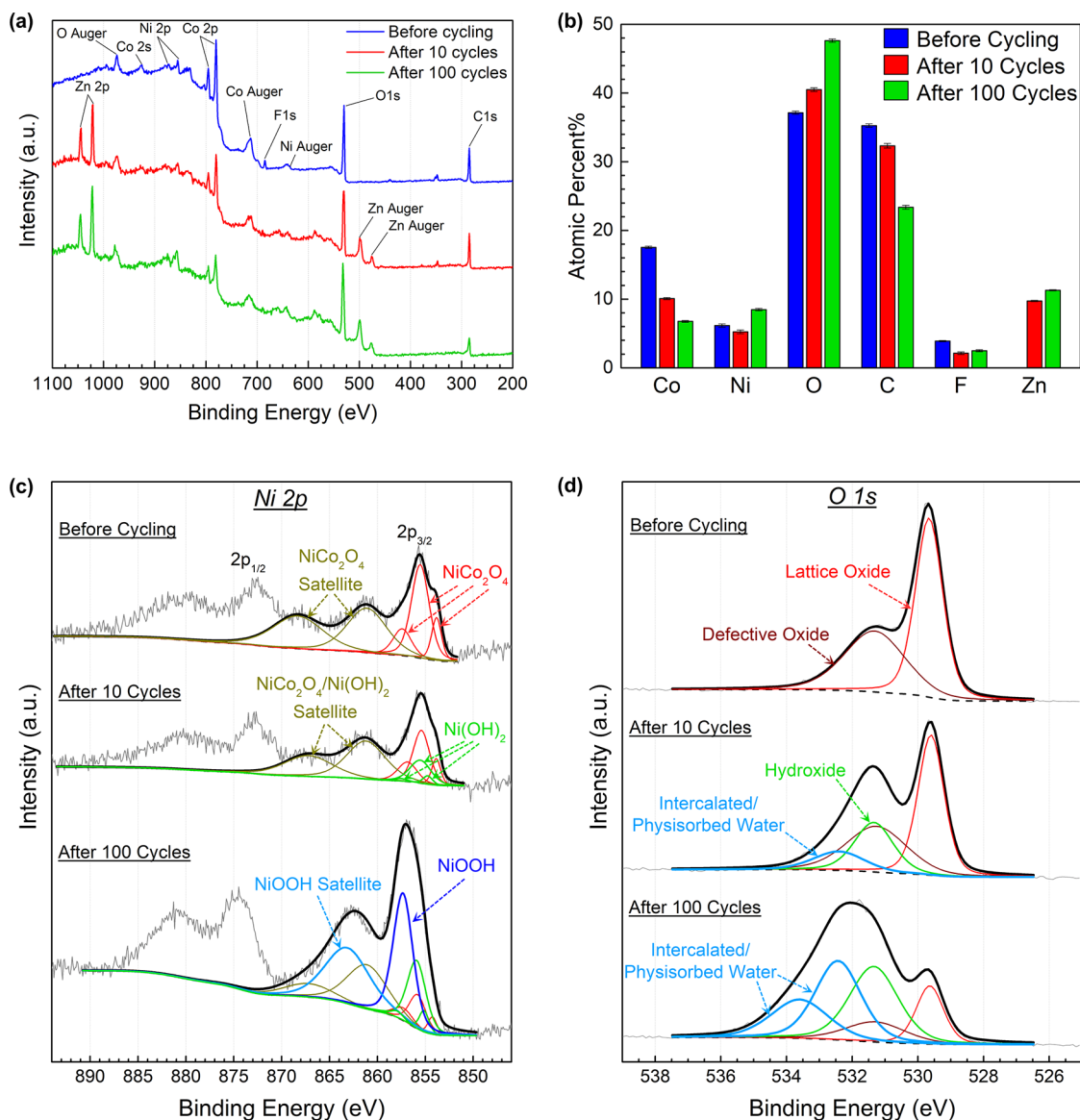


Figure 7. XPS analysis of the nickel-based gas diffusion electrode before and after 10 and 100 galvanostatic oxidation/reduction cycles (Table 1): (a) survey spectra, (b) quantified chemical composition of electrode surfaces where the error bars represent the uncertainty (one standard deviation) of the quantified measurement,^{65,66} (c) high-resolution deconvoluted Ni 2p spectra, and (d) high-resolution deconvoluted O 1s spectra.

accurate fitting. After 100 cycles, the lattice oxide peak was significantly reduced while the hydroxide and water peaks were enhanced. An additional higher-binding energy water peak that has been previously noted in oxyhydroxide compounds⁶⁷ was also needed to fit the spectral data. $\text{Zn}(\text{OH})_4^{2-}$ dissolved in this bound or intercalated water within the nickel (oxy)hydroxide film likely gave rise to the metastable ϵ - $\text{Zn}(\text{OH})_2$ phase observed in XRD analysis (Figure 6). More importantly, intercalated water in the nickel (oxy)hydroxide film might play a role in preventing mass transfer of oxygen to the underlying NiCo_2O_4 catalyst, thus causing reduced ORR kinetics after cycling. Regardless, the nickel (oxy)hydroxide film observed with SEM and XPS is proposed to be the principal cause of potential degradation observed during galvanostatic cycling, since it likely increases the resistance of oxygen diffusion to the NiCo_2O_4 catalyst.

For deeper electrochemical insight on the increasing ORR overpotentials, galvanostatic cycling with EIS measurements at a reduction current of 10 mA cm^{-2} were conducted according

to Table 2 on a new gas diffusion electrode. The first important observation is that the ohmic resistance, indicated by the high-frequency real impedance intercepts (Figure 8 inset), did not substantially increase as cycling progressed. This resistance was

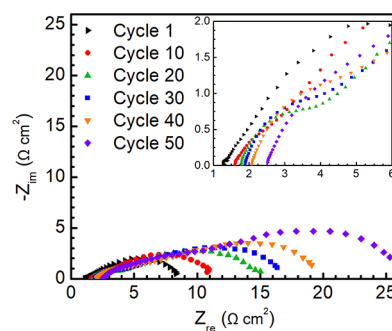


Figure 8. Galvanostatic EIS plots (procedure per Table 2) for nickel-based gas diffusion electrode.

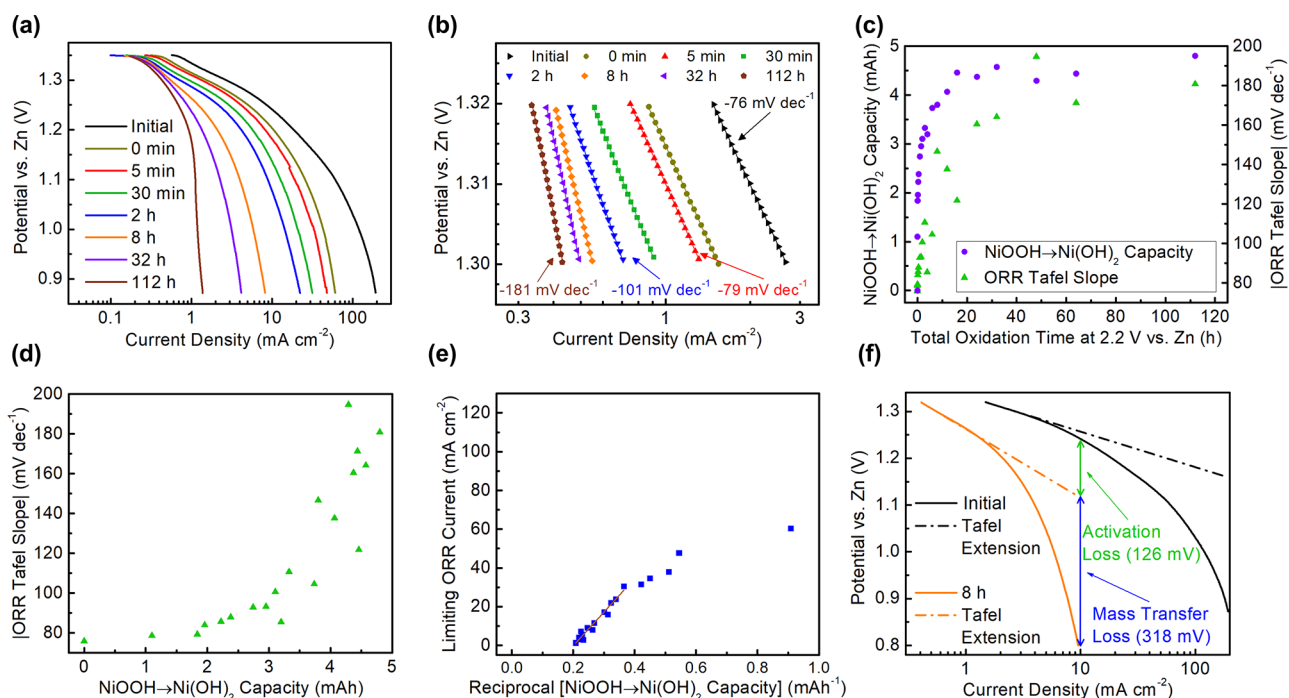


Figure 9. Cyclic potentiodynamic polarization (procedure per Table 3) for nickel-based gas diffusion electrode: (a) Full IR-corrected ORR polarization curves and (b) ORR Tafel plots after various total oxidation times at 2.2 V, (c) dependence of NiOOH → Ni(OH)₂ capacity and ORR Tafel slope magnitude on the total oxidation time at 2.2 V, (d) dependence of ORR Tafel slope magnitude on NiOOH → Ni(OH)₂ capacity, (e) dependence of limiting ORR current on the reciprocal of NiOOH → Ni(OH)₂ capacity with line of best fit over linear region, and (f) ORR polarization curves before and after oxidation at 2.2 V for 8 h with extrapolation of the Tafel regions.

1.3 Ω cm² during the first cycle and 2.5 Ω cm² during the 50th cycle, corresponding to a very minor 12 mV increase of the ohmic drop at 10 mA cm⁻². Therefore, ohmic resistance (within the electrolyte, electrode or current collectors) could not have accounted for the large ORR potential loss observed in Figure 4a,b,d. The EIS spectra in Figure 8 appeared as two depressed semicircles, especially visible after higher cycle numbers, which is characteristic of porous electrodes.⁷⁷ Similar EIS spectra for gas diffusion electrodes have previously been modeled by a modified Randles circuit with one or more finite diffusion elements in series with the charge transfer resistance term.^{34,77,78} In this case, the low-frequency (rightmost) semicircle appeared to experience the most growth as cycling progressed. This suggests that increased diffusion resistance was responsible for most of the ORR potential loss observed in Figure 4a,b,d.⁷⁷

Cyclic potentiodynamic polarization experiments were conducted on the gas diffusion electrode to directly investigate the role of activation loss (measured by analysis of the Tafel region) and mass transfer loss (measured by the limiting currents). The IR-corrected ORR polarization curves, which were measured as part of the procedure outlined in Table 3, are displayed in Figure 9a. Figure 9b shows the Tafel region of the ORR polarization curves measured after different cumulative times of oxidation at 2.2 V. Tafel slopes observed for the ORR on spinel catalysts in alkaline electrolytes have a minimum value of approximately 40 mV dec⁻¹.^{79–81} This is consistent with a theoretical value of 39 mV dec⁻¹ ($2.303RT/\alpha F$, $\alpha = 1.5$),⁸² which is predicted for the ORR where the second electron-transfer step of the 4-electron pathway is rate-determining.⁸³ Doubled Tafel slopes are often observed on porous air electrodes due to oxygen transport limitations within porous aggregates,^{54,55,82,84} which would explain the

initial value of 76 mV dec⁻¹ observed in Figure 9b. The shift from the normal Tafel slope to the double Tafel slope likely occurred at a potential above the polarization range.

The first oxidation cycle (oxidized at 10 mA cm⁻² until reaching the cutoff of 1.95 V and skipping step 8 of Table 3) and second oxidation cycle (5 min at 2.2 V) caused the NiOOH/Ni(OH)₂ capacity to quickly increase from 0 to 1.1 and 1.8 mAh, respectively (Figure 9c). The Tafel slope remained close (79 mV dec⁻¹) to its initial value after 5 min of charging (Figure 9b); however, the recorded current densities shifted negatively, which likely indicates the transition to a doubled Tafel slope occurred at a higher potential compared to the initial polarization curve. This could be attributed to the nickel (oxy)hydroxide film growing inside the pores of the catalyst-coated nickel aggregates, causing increased internal oxygen diffusion resistance and thus a transition to a doubled Tafel slope at a smaller ORR overpotential.⁵⁵ After greater oxidation time periods, currents in the Tafel region were further reduced. While this is partially explained by a further negative shift of the Tafel regions, it was also due to increasing Tafel slope magnitudes which reached nearly 200 mV dec⁻¹ (Figure 9b). The dependence of both the NiOOH/Ni(OH)₂ capacity and ORR Tafel slope magnitude on the total oxidation time is shown in Figure 9c. Both values displayed relatively rapid increases within the first 8 h of oxidation at 2.2 V, followed by more gradual increases during the remaining 104 h.

An increasing Tafel slope could be attributed to two different factors, which in turn may be at least partially attributed to the growing nickel (oxy)hydroxide film. First, if the rate-determining step of the ORR is changed from the second electron transfer step to the previous step (between the first and second electron transfers) involving adsorbed

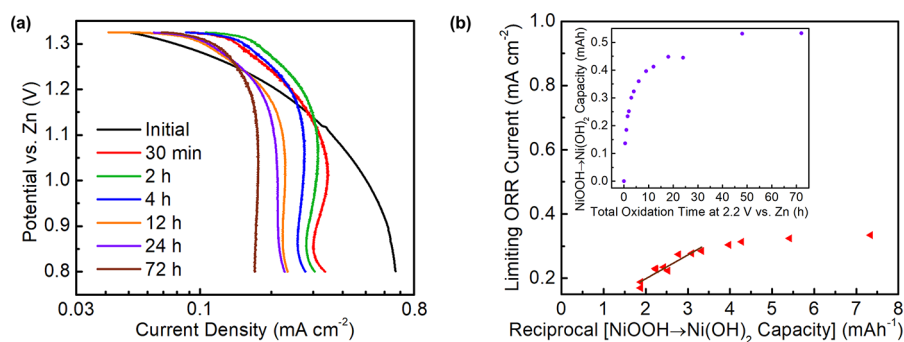


Figure 10. Cyclic potentiodynamic polarization (procedure per Table 3) for nickel-based thin-layer electrode: (a) full IR-corrected ORR polarization curves and (b) dependence of limiting ORR current on the reciprocal of NiOOH \rightarrow Ni(OH)₂ capacity with line of best fit over linear region (inset: dependence of NiOOH \rightarrow Ni(OH)₂ capacity on the total oxidation time at 2.2 V).

superoxide exchange with a surface hydroxide on the catalyst surface,⁸³ the theoretical Tafel slope would change from 39 to 59 mV dec⁻¹ ($2.303RT/\alpha F$, $\alpha = 1.0$),⁸² or an increase of 1.5 times. This may be caused by the increased presence of Ni(OH)₂ or NiOOH surfaces, which have relatively slow redox reaction kinetics to support superoxide exchange.⁸⁵ Second, the Tafel slope (already presumed to be doubled due to oxygen transport limitations, as mentioned above) could be doubled again if both oxygen and ionic transport resistances become significant within the porous nickel aggregates of the electrode.⁵⁵ Ionic transport limitations within the porous aggregates are expected to occur due to reduced pore sizes between the Ni particles resulting from growth of the nickel (oxy)hydroxide film. Contributions from both factors would be needed to explain the Tafel slope increases observed in Figure 9b, since the first factor or second factor alone would only result in a maximum Tafel slope of 118 mV dec⁻¹ ($2 \times 2.303RT/\alpha F$, $\alpha = 1.0$) or 158 mV dec⁻¹ ($2 \times 2 \times 2.303RT/\alpha F$, $\alpha = 1.5$), respectively.^{55,82} Figure 9d displays the relationship between the ORR Tafel slope magnitude and the NiOOH/Ni(OH)₂ capacity, where a relatively minor positive dependence is observed within the first 3 mAh of growth followed by an approximate doubling of the Tafel slope as the NiOOH/Ni(OH)₂ capacity approaches its maximum (limiting) value. The doubling of the Tafel slope during the latter period is consistent with the explanation of it being caused by significant ionic transport limitations (second factor above); this is reasoned because ionic transfer limitations are also likely to cause the nickel (oxy)hydroxide film's growth to become limited during this period, since hydroxide ions are required for the nickel oxidation reaction (eq 3) to continue. This leaves the initial Tafel slope increase within the first 3 mAh of growth to be explained by a change of the rate-determining step (first factor above). Thus, from this analysis it is very likely that the nickel (oxy)hydroxide film plays a significant role in increasing activation losses of the nickel-based air electrode.

The ORR polarization curves in Figure 9a also display substantial reductions of the limiting current as the oxidation time is increased, revealing significantly increased mass transfer losses. On the basis of the SEM and XPS observations that the nickel (oxy)hydroxide film grows otop of the NiCo₂O₄ catalyst, increased mass transfer losses are expected since oxygen must diffuse through an increasingly thicker film before undergoing reduction at the catalyst surface. If the nickel (oxy)hydroxide film is the dominating source of diffusion resistance, the limiting current will be inversely proportional to the film's thickness.^{54,86} To confirm this, the limiting current

measured at 0.875 V vs Zn was plotted against the reciprocal of the measured NiOOH/Ni(OH)₂ capacity (which is assumed to be proportional to its thickness) in Figure 9e. A linear correlation was indeed observed at high capacities (low reciprocal values), indicating that the nickel (oxy)hydroxide film was likely the dominant source of diffusion resistance when it became significantly thick. At low nickel (oxy)hydroxide thickness (high reciprocal capacity), deviation of the measured limiting currents from the linear pattern indicates that the porous PTFE/electrolyte/gas network in the air electrode (Figure 1a) was the initial dominant source of diffusion resistance.

Figure 9f compares the ORR polarization curves before oxidation (initial) and after 8 h of oxidation, including dashed lines for extrapolation of the Tafel slopes. This enables a comparison of the relative contributions of activation and mass transfer overpotential at different current densities. At 10 mA cm⁻², which was the current density for the galvanostatic oxidation/reduction experiments (Figure 4), mass transfer losses are the more significant source of overpotential after 8 h. After longer oxidation times, mass transfer losses are even more significant. Therefore, the rapid potential loss observed after 50 cycles in Figure 4d likely occurred when the limiting current approached and fell below 10 mA cm⁻². Even for shorter oxidation times, mass transfer losses were always responsible for at least 65% of the total potential loss from the initial performance at 10 mA cm⁻², indicating the high significance of performance degradation caused by the nickel (oxy)hydroxide film growing otop of the catalyst.

Although the linear portion of Figure 9e strongly suggested that the nickel (oxy)hydroxide film was the dominant source of mass transfer losses, other time-dependent sources such as electrolyte flooding into the gas diffusion channels or carbonate precipitation within the electrode pores could potentially contribute to diffusion resistance. Therefore, a similar experiment using a thin-layer electrode and the cell shown in Figure 1c was performed to further investigate mass transfer losses. The thin-layer electrode (150 μ m thick) minimizes the importance of through-thickness oxygen diffusion in comparison to the relatively thick (1000 μ m) gas diffusion electrode. Also, the only source of oxygen in this cell is dissolved in the electrolyte (i.e., no gas phase oxygen), meaning that mass transfer losses caused by electrolyte flooding into gas channels is not applicable. Moreover, since the oxygen and water reactants arrive from the same side of the electrode in this case, the ORR should be concentrated on the surface of the thin-layer electrode, which further minimizes the

importance of through-thickness oxygen diffusion. Finally, the large volume of circulating electrolyte means that carbonates are unlikely to precipitate inside the electrode pores. Therefore, if the same relationship between limiting current and reciprocal $\text{NiOOH}/\text{Ni}(\text{OH})_2$ capacity is observed in this experiment, mass transfer losses can be more definitively attributed to oxygen diffusion limitations through the nickel (oxy)hydroxide film.

Figure 10a shows the ORR polarization curves for the thin-layer electrode after various cumulative times of oxidation at 2.2 V vs Zn. Much smaller limiting currents were observed in comparison to the gas diffusion electrode, highlighting the importance of exposure to the oxygen gas phase. It should be noted that Tafel slopes could not be measured from most of these curves since mass transfer losses appeared to dominate even at low overpotentials. Despite the much lower limiting currents, a similar trend of decreasing limiting currents with higher oxidation times was seen, while the inset of Figure 10b shows a similar relationship between the $\text{NiOOH}/\text{Ni}(\text{OH})_2$ capacity and total oxidation time. Most importantly, Figure 10b displays the same linear correlation between the limiting current and reciprocal of the $\text{NiOOH}/\text{Ni}(\text{OH})_2$ capacity at high capacity values. The deviation of limiting currents from the linear pattern at low capacity values means that, in this case, the diffusion of dissolved oxygen through the electrolyte was the limiting factor prior to significant growth of the nickel (oxy)hydroxide film. Since other possible sources of mass transfer loss in the gas diffusion electrode can be ruled out in this experiment, the same relationships observed in Figure 9e and Figure 10b points to the nickel (oxy)hydroxide film as the most significant source of mass transfer losses in both electrodes. Since the nickel (oxy)hydroxide film grows most rapidly at high potentials (i.e., during OER or charging of a zinc–air battery), the majority of voltage loss in each cycling experiment was likely dictated by total charging time at a given potential and not by other cycling parameters such as the depth of discharge.

To summarize, the ORR potential losses observed during cycling of the nickel-based air electrode investigated in this work were caused by a combination of activation and mass transfer losses. Both losses were mainly attributed to the growth of the nickel (oxy)hydroxide film, which is shown schematically for an aggregate of catalyst-coated nickel particles in Figure 11 (actual aggregates could potentially be

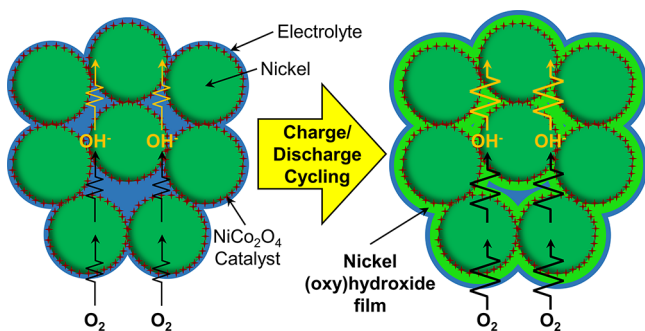


Figure 11. Schematic representation of an electrolyte-flooded agglomerate of catalyst-coated nickel particles. The nickel oxy(hydroxide) film growth resulting from prolonged oxidation causes increased oxygen and ionic transport resistance within the aggregate and increased oxygen transport resistance from the outside to the inside of the aggregate.

much more than eight particles as shown here). Activation losses were associated with a steeper and negatively shifted Tafel slope, which are caused by increased resistance to oxygen and ionic transport within the aggregate due to film growth inside the pores between the particles. The increased Tafel slope was also attributed to rate limitations of the adsorbed superoxide exchange step in the ORR mechanism, which might also be influenced by nickel (oxy)hydroxide film growth. Mass transfer losses were caused by increased oxygen transport resistance from the gas diffusion channels to the inside of the aggregate due to the nickel (oxy)hydroxide film growth on the outer nickel surfaces. At 10 mA cm^{-2} , mass transfer losses were the dominant source of ORR overpotential. These findings are applicable not only to nickel-supported catalysts, but to any catalyst system involving a metal component where an oxidation film could grow from its surface and block a nearby catalyst site (possibly the metal itself) from access to reactants.

The results of this investigation have important implications for the design of nickel-based bifunctional air electrodes with improved stability, as well as air electrodes based on other porous networks of metals which may form passivating films. First, the size of the nickel particle aggregates should be reduced; this would shorten the diffusion lengths within the aggregate and mitigate the activation losses from higher effective diffusion coefficients arising from film growth within the aggregate. This could be accomplished by improving the dispersion of nickel and PTFE to minimize nickel particle aggregation during electrode preparation.⁸⁷ While the influence of the nickel particle size itself is not clear, we suspect the use of larger particles could help minimize aggregation, although larger particles could also result in a significantly lower surface area for catalyst deposition. For mitigating mass transfer losses, the deposited catalyst could be engineered with a high aspect ratio (e.g., nanowire morphology^{19,88}) such that it extends far enough from the nickel support to maintain direct exposure to the electrolyte/gas phase after the passivating film growth begins to slow down. Alternatively, a physical mixture of nickel and catalyst particles (rather than catalyst-coated nickel particles employed in this work) could provide greater separation between the two materials, thus avoiding total (oxy)hydroxide film coverage of the catalyst. However, this could lead to significant ohmic resistance losses if the (oxy)hydroxide film grows between the nickel and catalyst particles. In this case, incorporating a small amount of nonfilm-forming conductive additives (i.e., carbon or graphite) in the air electrode to maintain electron-conductive interfaces⁵⁰ may be beneficial, if the relatively minor carbonate generation from the corrosion of the distributed carbon is tolerable. Finally, it may be possible to completely replace metal supports with metal oxide/hydroxide supports if their conductivity could be sufficiently increased,^{89,90} since the growth of oxidation films would not apply in this case. Certainly, the rechargeability of carbon-free or low-carbon air electrodes can be greatly improved by optimizing these structural and compositional factors.

CONCLUSIONS

In this work, the nature and underlying mechanism of nickel-based air electrode performance loss was investigated within rechargeable zinc–air batteries. It was shown that increased ORR overpotential after extended battery cycling was caused by a combination of activation and mass transfer losses, with the latter more significant at a current density of 10 mA cm^{-2} .

Electron microscopy and X-ray photoelectron spectroscopy revealed the growth of a nickel (oxy)hydroxide film overtop of the NiCo₂O₄ catalyst, which impeded oxygen diffusion and was the dominant source of mass transfer losses after it grew significantly thick. Nickel (oxy)hydroxide film growth within the pores of the catalyst-coated nickel particle aggregates also likely contributed to higher activation losses evidenced by steeper and negatively shifted Tafel slopes. The diagnostic methods in this work shed light on various strategies for mitigating performance loss caused by the (oxy)hydroxide film growth. Implementing these strategies could lead to high-energy density rechargeable zinc–air batteries with long cycle life and calendar life.

AUTHOR INFORMATION

Corresponding Author

*(Z.C.) E-mail: zhwchen@uwaterloo.ca. Telephone: 1-519-888-4567, Ext. 38664. Fax: 1-519-746-4979.

ORCID

Zachary P. Cano: 0000-0002-2433-297X

Michael Fowler: 0000-0002-9761-0336

Zhongwei Chen: 0000-0003-3463-5509

Present Address

[†]Department: Chemical Engineering, Stanford University, 450 Serra Mall, Stanford, CA 94305

Notes

The authors declare no competing financial interest.

ACKNOWLEDGMENTS

The authors would like to thank the Natural Sciences and Engineering Research Council of Canada (NSERC) and the University of Waterloo for financial support.

REFERENCES

- (1) Gröger, O.; Gasteiger, H. A.; Suchsland, J.-P. Review—Electromobility: Batteries or Fuel Cells? *J. Electrochem. Soc.* **2015**, *162*, A2605–A2622.
- (2) Malhotra, A.; Battke, B.; Beuse, M.; Stephan, A.; Schmidt, T. Use Cases for Stationary Battery Technologies: A Review of the Literature and Existing Projects. *Renewable Sustainable Energy Rev.* **2016**, *56*, 705–721.
- (3) Khan, P. A.; Venkatesh, B. Economic Analysis of Chemical Energy Storage Technologies. *Smart City 360°* **2016**, *166*, 277–291.
- (4) Deign, J. Eos grapples with scale-up challenges on route to DC cost of \$95 per kWh <http://energystoragereport.info/eos-grapples-scale-challenges/> (accessed Dec 22, 2017).
- (5) Passaniti, J.; Carpenter, D.; McKenzie, R. Button Cell Batteries: Silver Oxide-Zinc and Zinc-Air Systems. In *Linden's Handbook of Batteries*, 4th ed.; McGraw Hill Professional: New York, 2010.
- (6) Sieminski, D. Recent Advances in Rechargeable Zinc-Air Battery Technology. *The Twelfth Annual Battery Conference on Applications and Advances* **1997**, BCAA-97, 171–180.
- (7) Larsson, F.; Rytinki, A.; Ahmed, I.; Albinsson, I.; Mellander, B.-E. Overcurrent Abuse of Primary Prismatic Zinc–Air Battery Cells Studying Air Supply Effects on Performance and Safety Shut-Down. *Batteries* **2017**, *3*, 1–10.
- (8) Fu, J.; Cano, Z. P.; Park, M. G.; Yu, A.; Fowler, M.; Chen, Z. Electrically Rechargeable Zinc–Air Batteries: Progress, Challenges, and Perspectives. *Adv. Mater.* **2017**, *29*, 1604685.
- (9) Cano, Z. P.; Banham, D.; Ye, S.; Hintennach, A.; Lu, J.; Fowler, M.; Chen, Z. Batteries and Fuel Cells for Emerging Electric Vehicle Markets. *Nat. Energy* **2018**, *3*, 279–289.
- (10) Kammen, D. M.; Sunter, D. A. City-Integrated Renewable Energy for Urban Sustainability. *Science* **2016**, *352*, 922–928.

(11) Lee, J.-S.; Tai Kim, S.; Cao, R.; Choi, N.-S.; Liu, M.; Lee, K. T.; Cho, J. Metal–Air Batteries with High Energy Density: Li–Air versus Zn–Air. *Adv. Energy Mater.* **2011**, *1*, 34–50.

(12) Cheng, F.; Chen, J. Metal–Air Batteries: From Oxygen Reduction Electrochemistry to Cathode Catalysts. *Chem. Soc. Rev.* **2012**, *41*, 2172–2192.

(13) Li, Y.; Dai, H. Recent Advances in Zinc–Air Batteries. *Chem. Soc. Rev.* **2014**, *43*, 5257–5275.

(14) Wang, Z.-L.; Xu, D.; Xu, J.-J.; Zhang, X.-B. Oxygen Electrocatalysts in Metal–Air Batteries: From Aqueous to Non-aqueous Electrolytes. *Chem. Soc. Rev.* **2014**, *43*, 7746–7786.

(15) Lee, D. U.; Xu, P.; Cano, Z. P.; Kashkooli, A. G.; Park, M. G.; Chen, Z. Recent Progress and Perspectives on Bi-Functional Oxygen Electrocatalysts for Advanced Rechargeable Metal–Air Batteries. *J. Mater. Chem. A* **2016**, *4*, 7107–7134.

(16) Davari, E.; Ivey, D. G. Bifunctional Electrocatalysts for Zn–Air Batteries. *Sustain. Energy Fuels* **2018**, *2*, 39–67.

(17) Song, W.; Ren, Z.; Chen, S.-Y.; Meng, Y.; Biswas, S.; Nandi, P.; Elsen, H. A.; Gao, P.-X.; Suib, S. L. Ni- and Mn-Promoted Mesoporous Co₃O₄: A Stable Bifunctional Catalyst with Surface-Structure-Dependent Activity for Oxygen Reduction Reaction and Oxygen Evolution Reaction. *ACS Appl. Mater. Interfaces* **2016**, *8*, 20802–20813.

(18) Han, X.; Wu, X.; Zhong, C.; Deng, Y.; Zhao, N.; Hu, W. NiCo₂S₄ Nanocrystals Anchored on Nitrogen-Doped Carbon Nanotubes as a Highly Efficient Bifunctional Electrocatalyst for Rechargeable Zinc-Air Batteries. *Nano Energy* **2017**, *31*, 541–550.

(19) Ren, J.-T.; Yuan, G.-G.; Weng, C.-C.; Yuan, Z.-Y. Rationally Designed Co₃O₄–C Nanowire Arrays on Ni Foam Derived From Metal Organic Framework as Reversible Oxygen Evolution Electrodes with Enhanced Performance for Zn–Air Batteries. *ACS Sustainable Chem. Eng.* **2018**, *6*, 707–718.

(20) Han, X.; He, G.; He, Y.; Zhang, J.; Zheng, X.; Li, L.; Zhong, C.; Hu, W.; Deng, Y.; Ma, T.-Y. Engineering Catalytic Active Sites on Cobalt Oxide Surface for Enhanced Oxygen Electrocatalysis. *Adv. Energy Mater.* **2018**, *8*, 1702222.

(21) Zhu, S.; Chen, Z.; Li, B.; Higgins, D.; Wang, H.; Li, H.; Chen, Z. Nitrogen-Doped Carbon Nanotubes as Air Cathode Catalysts in Zinc-Air Battery. *Electrochim. Acta* **2011**, *56*, 5080–5084.

(22) Lee, D. U.; Park, H. W.; Higgins, D.; Nazar, L.; Chen, Z. Highly Active Graphene Nanosheets Prepared via Extremely Rapid Heating as Efficient Zinc-Air Battery Electrode Material. *J. Electrochem. Soc.* **2013**, *160*, F910–F915.

(23) Ng, J. W. D.; Tang, M.; Jaramillo, T. F. A Carbon-Free, Precious-Metal-Free, High-Performance O₂ Electrode for Regenerative Fuel Cells and Metal–Air Batteries. *Energy Environ. Sci.* **2014**, *7*, 2017–2024.

(24) Lee, D. U.; Fu, J.; Park, M. G.; Liu, H.; Ghorbani Kashkooli, A.; Chen, Z. Self-Assembled NiO/Ni(OH)₂ Nanoflakes as Active Material for High-Power and High-Energy Hybrid Rechargeable Battery. *Nano Lett.* **2016**, *16*, 1794–1802.

(25) Li, P.-C.; Chien, Y.-J.; Hu, C.-C. Novel Configuration of Bifunctional Air Electrodes for Rechargeable Zinc–Air Batteries. *J. Power Sources* **2016**, *313*, 37–45.

(26) Ma, C.; Xu, N.; Qiao, J.; Jian, S.; Zhang, J. Facile Synthesis of NiCo₂O₄ Nanosphere-Carbon Nanotubes Hybrid as an Efficient Bifunctional Electrocatalyst for Rechargeable Zn–Air Batteries. *Int. J. Hydrogen Energy* **2016**, *41*, 9211–9218.

(27) Shteinberg, G. V.; Dribinsky, A. V.; Kukushkina, I. A.; Mokrousov, L. N.; Bagotzky, V. S. Investigation of the Carbon-Oxygen (Air) Electrode. *J. Electroanal. Chem. Interfacial Electrochem.* **1984**, *180*, 619–637.

(28) Tomantschger, K.; Kordesch, K. V. Structural Analysis of Alkaline Fuel Cell Electrodes and Electrode Materials. *J. Power Sources* **1989**, *25*, 195–214.

(29) Dicks, A. L. The Role of Carbon in Fuel Cells. *J. Power Sources* **2006**, *156*, 128–141.

(30) Kordesch, K.; Hacker, V. Stack Materials and Design. In *Handbook of Fuel Cells*; John Wiley & Sons, Ltd.: Hoboken, NJ, 2010.

- (31) Neburchilov, V.; Wang, H.; Martin, J. J.; Qu, W. A Review on Air Cathodes for Zinc–Air Fuel Cells. *J. Power Sources* **2010**, *195*, 1271–1291.
- (32) Ross, P. N.; Sokol, H. The Corrosion of Carbon Black Anodes in Alkaline Electrolyte I. Acetylene Black and the Effect of Cobalt Catalyzation. *J. Electrochem. Soc.* **1984**, *131*, 1742–1750.
- (33) Staud, N.; Ross, P. N. The Corrosion of Carbon Black Anodes in Alkaline Electrolyte II. Acetylene Black and the Effect of Oxygen Evolution Catalysts on Corrosion. *J. Electrochem. Soc.* **1986**, *133*, 1079–1084.
- (34) Müller, S.; Holzer, F.; Arai, H.; Haas, O. A Study of Carbon-Catalyst Interaction in Bifunctional Air Electrodes for Zinc–Air Batteries. *J. New Mater. Electrochem. Syst.* **1999**, *2*, 227–232.
- (35) Velraj, S.; Zhu, J. H. Cycle Life Limit of Carbon-Based Electrodes for Rechargeable Metal–Air Battery Application. *J. Electroanal. Chem.* **2015**, *736*, 76–82.
- (36) Ma, Z.; Pei, P.; Wang, K.; Wang, X.; Xu, H.; Liu, Y.; et al. Degradation Characteristics of Air Cathode in Zinc Air Fuel Cells. *J. Power Sources* **2015**, *274*, 56–64.
- (37) Thippiani, T.; Mandal, S.; Wang, G.; Ramani, V. K.; Kothandaraman, R. Probing Oxygen Reduction and Oxygen Evolution Reactions on Bifunctional Non-Precious Metal Catalysts for Metal–Air Batteries. *RSC Adv.* **2016**, *6*, 71122–71133.
- (38) Kinoshita, K. Carbons. In *Handbook of Battery Materials*; Daniel, C., Besenhard, J. O., Eds.; Wiley-VCH Verlag GmbH & Co. KGaA: Weinheim, Germany, 2011; pp 269–284.
- (39) Vanýsek, P. Electrochemical Series. In *CRC Handbook of Chemistry and Physics*, 97th ed.; CRC Press: Boca Raton, FL, 2016.
- (40) Ross, P. N.; Sattler, M. The Corrosion of Carbon Black Anodes in Alkaline Electrolyte III. The Effect of Graphitization on the Corrosion Resistance of Furnace Blacks. *J. Electrochem. Soc.* **1988**, *135*, 1464–1470.
- (41) Staud, N.; Sokol, H.; Ross, P. N. The Corrosion of Carbon Black Anodes in Alkaline Electrolyte IV. Current Efficiencies for Oxygen Evolution from Metal Oxide-Impregnated Graphitized Furnace Blacks. *J. Electrochem. Soc.* **1989**, *136*, 3570–3576.
- (42) Müller, S.; Striebel, K.; Haas, O. $\text{La}_{0.6}\text{Ca}_{0.4}\text{CoO}_3$: A Stable and Powerful Catalyst for Bifunctional Air Electrodes. *Electrochim. Acta* **1994**, *39*, 1661–1668.
- (43) Drillet, J.-F.; Holzer, F.; Kallis, T.; Müller, S.; Schmidt, V. M. Influence of CO_2 on the Stability of Bifunctional Oxygen Electrodes for Rechargeable Zinc/Air Batteries and Study of Different CO_2 Filter Materials. *Phys. Chem. Chem. Phys.* **2001**, *3*, 368–371.
- (44) Gülzow, E.; Wagner, N.; Schulze, M. Preparation of Gas Diffusion Electrodes with Silver Catalysts for Alkaline Fuel Cells. *Fuel Cells* **2003**, *3*, 67–72.
- (45) Bidault, F.; Kucernak, A. A Novel Cathode for Alkaline Fuel Cells Based on a Porous Silver Membrane. *J. Power Sources* **2010**, *195*, 2549–2556.
- (46) Wittmaier, D.; Wagner, N.; Friedrich, K. A.; Amin, H. M. A.; Baltruschat, H. Modified Carbon-Free Silver Electrodes for the Use as Cathodes in Lithium–Air Batteries with an Aqueous Alkaline Electrolyte. *J. Power Sources* **2014**, *265*, 299–308.
- (47) Li, X.; Pletcher, D.; Russell, A. E.; Walsh, F. C.; Wills, R. G. A.; Gorman, S. F.; Price, S. W. T.; Thompson, S. J. A Novel Bifunctional Oxygen GDE for Alkaline Secondary Batteries. *Electrochem. Commun.* **2013**, *34*, 228–230.
- (48) Price, S. W. T.; Thompson, S. J.; Li, X.; Gorman, S. F.; Pletcher, D.; Russell, A. E.; Walsh, F. C.; Wills, R. G. A. The Fabrication of a Bifunctional Oxygen Electrode without Carbon Components for Alkaline Secondary Batteries. *J. Power Sources* **2014**, *259*, 43–49.
- (49) Liu, X.; Park, M.; Kim, M. G.; Gupta, S.; Wang, X.; Wu, G.; Cho, J. High-Performance Non-Spinel Cobalt–Manganese Mixed Oxide-Based Bifunctional Electrocatalysts for Rechargeable Zinc–Air Batteries. *Nano Energy* **2016**, *20*, 315–325.
- (50) Park, M. G.; Lee, D. U.; Seo, M. H.; Cano, Z. P.; Chen, Z. 3D Ordered Mesoporous Bifunctional Oxygen Catalyst for Electrically Rechargeable Zinc–Air Batteries. *Small* **2016**, *12*, 2707–2714.
- (51) Park, J.; Risch, M.; Nam, G.; Park, M.; Shin, T. J.; Park, S.; Kim, M. G.; Shao-Horn, Y.; Cho, J. Single Crystalline Pyrochlore Nanoparticles with Metallic Conduction as Efficient Bi-Functional Oxygen Electrocatalysts for Zn–Air Batteries. *Energy Environ. Sci.* **2017**, *10*, 129–136.
- (52) Pichler, B.; Weinberger, S.; Rešćec, L.; Grimmer, I.; Gebetsroither, F.; Bitschnau, B.; Hacker, V. Bifunctional Electrode Performance for Zinc–Air Flow Cells with Pulse Charging. *Electrochim. Acta* **2017**, *251*, 488–497.
- (53) Giner, J.; Hunter, C. The Mechanism of Operation of the Teflon-Bonded Gas Diffusion Electrode: A Mathematical Model. *J. Electrochem. Soc.* **1969**, *116*, 1124–1130.
- (54) Björnbohm, P. Modelling of a Double-Layered PTFE-Bonded Oxygen Electrode. *Electrochim. Acta* **1987**, *32*, 115–119.
- (55) Perry, M. L.; Newman, J.; Cairns, E. J. Mass Transport in Gas-Diffusion Electrodes: A Diagnostic Tool for Fuel-Cell Cathodes. *J. Electrochem. Soc.* **1998**, *145*, 5–15.
- (56) Bidault, F.; Brett, D. J. L.; Middleton, P. H.; Brandon, N. P. Review of Gas Diffusion Cathodes for Alkaline Fuel Cells. *J. Power Sources* **2009**, *187*, 39–48.
- (57) Chamoun, M.; Hertzberg, B. J.; Gupta, T.; Davies, D.; Bhadra, S.; Van Tassel, B.; Erdonmez, C.; Steingart, D. A. Hyper-Dendritic Nanoporous Zinc Foam Anodes. *NPG Asia Mater.* **2015**, *7*, e178.
- (58) Watanabe, K.; Kikuoka, T.; Kumagai, N. Physical and Electrochemical Characteristics of Nickel Hydroxide as a Positive Material for Rechargeable Alkaline Batteries. *J. Appl. Electrochem.* **1995**, *25*, 219–226.
- (59) Cao, Y. L.; Yang, H. X.; Ai, X. P.; Xiao, L. F. The Mechanism of Oxygen Reduction on MnO_2 -Catalyzed Air Cathode in Alkaline Solution. *J. Electroanal. Chem.* **2003**, *557*, 127–134.
- (60) Yan, J.; Fan, Z.; Sun, W.; Ning, G.; Wei, T.; Zhang, Q.; Zhang, R.; Zhi, L.; Wei, F. Advanced Asymmetric Supercapacitors Based on $\text{Ni}(\text{OH})_2$ /Graphene and Porous Graphene Electrodes with High Energy Density. *Adv. Funct. Mater.* **2012**, *22*, 2632–2641.
- (61) Pletcher, D.; Li, X.; Price, S. W. T.; Russell, A. E.; Sönmez, T.; Thompson, S. J. Comparison of the Spinels Co_3O_4 and NiCo_2O_4 as Bifunctional Oxygen Catalysts in Alkaline Media. *Electrochim. Acta* **2016**, *188*, 286–293.
- (62) Medway, S. L.; Lucas, C. A.; Kowal, A.; Nichols, R. J.; Johnson, D. In Situ Studies of the Oxidation of Nickel Electrodes in Alkaline Solution. *J. Electroanal. Chem.* **2006**, *587*, 172–181.
- (63) Yamabi, S.; Imai, H. Growth Conditions for Wurtzite Zinc Oxide Films in Aqueous Solutions. *J. Mater. Chem.* **2002**, *12*, 3773–3778.
- (64) Qu, X.; Jia, D. Synthesis of Octahedral ZnO Mesoscale Superstructures via Thermal Decomposing Octahedral Zinc Hydroxide Precursors. *J. Cryst. Growth* **2009**, *311*, 1223–1228.
- (65) Harrison, K.; Hazell, L. B. The Determination of Uncertainties in Quantitative XPS/AES and Its Impact on Data Acquisition Strategy. *Surf. Interface Anal.* **1992**, *18*, 368–376.
- (66) Evans, S. Estimation of the Uncertainties Associated with XPS Peak Intensity Determination. *Surf. Interface Anal.* **1992**, *18*, 323–332.
- (67) Biesinger, M. C.; Payne, B. P.; Grosvenor, A. P.; Lau, L. W. M.; Gerson, A. R.; Smart, R. S. C. Resolving Surface Chemical States in XPS Analysis of First Row Transition Metals, Oxides and Hydroxides: Cr, Mn, Fe, Co and Ni. *Appl. Surf. Sci.* **2011**, *257*, 2717–2730.
- (68) Casella, I. G.; Guascito, M. R.; Sannazzaro, M. G. Voltammetric and XPS Investigations of Nickel Hydroxide Electrochemically Dispersed on Gold Surface Electrodes. *J. Electroanal. Chem.* **1999**, *462*, 202–210.
- (69) Schulze, M.; Reissner, R.; Lorenz, M.; Radke, U.; Schnurnberger, W. Photoelectron Study of Electrochemically Oxidized Nickel and Water Adsorption on Defined NiO Surface Layers. *Electrochim. Acta* **1999**, *44*, 3969–3976.
- (70) Gioia, D.; Laurita, A.; Di Bello, G.; Casella, I. G. Pulsed Electrochemical Deposition of Nickel Oxides on Multi-Walled Carbon Nanotubes from EDTA Alkaline Solutions: A SEM, XPS, and Voltammetric Characterization. *J. Solid State Electrochem.* **2016**, *20*, 3383–3391.

(71) Mansour, A. N.; Melendres, C. A. Characterization of Electrochemically Prepared γ -NiOOH by XPS. *Surf. Sci. Spectra* **1994**, *3*, 271–278.

(72) Kim, J.-G.; Pugmire, D. L.; Battaglia, D.; Langell, M. A. Analysis of the NiCo₂O₄ Spinel Surface with Auger and X-Ray Photoelectron Spectroscopy. *Appl. Surf. Sci.* **2000**, *165*, 70–84.

(73) Yang, J.; Liu, H.; Martens, W. N.; Frost, R. L. Synthesis and Characterization of Cobalt Hydroxide, Cobalt Oxyhydroxide, and Cobalt Oxide Nanodiscs. *J. Phys. Chem. C* **2010**, *114*, 111–119.

(74) Yuan, C.; Li, J.; Hou, L.; Zhang, X.; Shen, L.; Lou, X. W. D. Ultrathin Mesoporous NiCo₂O₄ Nanosheets Supported on Ni Foam as Advanced Electrodes for Supercapacitors. *Adv. Funct. Mater.* **2012**, *22*, 4592–4597.

(75) Marco, J. F.; Gancedo, J. R.; Gracia, M.; Gautier, J. L.; Ríos, E.; Berry, F. J. Characterization of the Nickel Cobaltite, NiCo₂O₄, Prepared by Several Methods: An XRD, XANES, EXAFS, and XPS Study. *J. Solid State Chem.* **2000**, *153*, 74–81.

(76) Payne, B. P.; Biesinger, M. C.; McIntyre, N. S. Use of Oxygen/Nickel Ratios in the XPS Characterisation of Oxide Phases on Nickel Metal and Nickel Alloy Surfaces. *J. Electron Spectrosc. Relat. Phenom.* **2012**, *185*, 159–166.

(77) Yuan, X.-Z.; Song, C.; Wang, H.; Zhang, J. EIS Equivalent Circuits. *Electrochemical Impedance Spectroscopy in PEM Fuel Cells: Fundamentals and Applications* **2010**, 139–192.

(78) Arai, H.; Müller, S.; Haas, O. AC Impedance Analysis of Bifunctional Air Electrodes for Metal-Air Batteries. *J. Electrochem. Soc.* **2000**, *147*, 3584–3591.

(79) De Koninck, M.; Marsan, B. Mn_xCu_{1-x}Co₂O₄ Used as Bifunctional Electrocatalyst in Alkaline Medium. *Electrochim. Acta* **2008**, *53*, 7012–7021.

(80) Liang, Y.; Li, Y.; Wang, H.; Zhou, J.; Wang, J.; Regier, T.; Dai, H. Co₃O₄ Nanocrystals on Graphene as a Synergistic Catalyst for Oxygen Reduction Reaction. *Nat. Mater.* **2011**, *10*, 780–786.

(81) Prabu, M.; Ketpang, K.; Shanmugam, S. Hierarchical Nanostructured NiCo₂O₄ as an Efficient Bifunctional Non-Precious Metal Catalyst for Rechargeable Zinc–Air Batteries. *Nanoscale* **2014**, *6*, 3173–3181.

(82) Soderberg, J. N.; Co, A. C.; Sirk, A. H. C.; Birss, V. I. Impact of Porous Electrode Properties on the Electrochemical Transfer Coefficient. *J. Phys. Chem. B* **2006**, *110*, 10401–10410.

(83) Ge, X.; Sumboja, A.; Wu, D.; An, T.; Li, B.; Goh, F. W. T.; Hor, T. S. A.; Zong, Y.; Liu, Z. Oxygen Reduction in Alkaline Media: From Mechanisms to Recent Advances of Catalysts. *ACS Catal.* **2015**, *5*, 4643–4667.

(84) Tilak, B. V.; Venkatesh, S.; Rangarajan, S. K. Polarization Characteristics of Porous Electrode Systems with Adsorbed Intermediates Participating in the Electrode Reaction A Study of Limiting Tafel Slopes. *J. Electrochem. Soc.* **1989**, *136*, 1977–1982.

(85) Liu, Z. X.; Li, Z. P.; Qin, H. Y.; Liu, B. H. Oxygen Reduction Reaction via the 4-Electron Transfer Pathway on Transition Metal Hydroxides. *J. Power Sources* **2011**, *196*, 4972–4979.

(86) Panero, S. Electrochemical Theory | Kinetics. *Encyclopedia of Electrochemical Power Sources* **2009**, 14–22.

(87) Masood, S. H.; Song, W. Q. Development of New Metal/Polymer Materials for Rapid Tooling Using Fused Deposition Modelling. *Mater. Eng.* **2004**, *25*, 587–594.

(88) Lee, D. U.; Choi, J.-Y.; Feng, K.; Park, H. W.; Chen, Z. Advanced Extremely Durable 3D Bifunctional Air Electrodes for Rechargeable Zinc-Air Batteries. *Adv. Energy Mater.* **2014**, *4*, 1301389.

(89) He, X.; Liu, Q.; Liu, J.; Li, R.; Zhang, H.; Chen, R.; Wang, J. Hierarchical NiCo₂O₄@NiCoAl-Layered Double Hydroxide Core/Shell Nanoforest Arrays as Advanced Electrodes for High-Performance Asymmetric Supercapacitors. *J. Alloys Compd.* **2017**, *724*, 130–138.

(90) Guo, X.; Zheng, T.; Ji, G.; Hu, N.; Xu, C.; Zhang, Y. Core/Shell Design of Efficient Electrocatalysts Based on NiCo₂O₄ Nanowires and NiMn LDH Nanosheets for Rechargeable Zinc–Air Batteries. *J. Mater. Chem. A* **2018**, *6*, 10243–10252.